



OPEN Structural characterization of uranium and lanthanide loaded borosilicate glass matrix

I. Tolnai¹, J. Osan¹, P. Jovari², F. Pinakidou³, A. Sulyok¹ & M. Fabian¹

Borosilicate glass is a potential candidate for high-level radioactive waste conditioning, thus understanding the effects caused by the combined presence of uranium and actinides within these matrices is of great importance. The glass matrix was simultaneously loaded with UO_3 and lanthanide oxides (CeO_2 , Nd_2O_3 , and Eu_2O_3) as chemical surrogates for actinides. Neutron diffraction in combination with Reverse Monte Carlo simulation confirmed that the basic glass structure is comprised of tetrahedral SiO_4 and BO_3/BO_4 units. X-ray absorption spectroscopy indicated the presence of Ce mainly as Ce^{III} and the co-existence of U^{V} and U^{VI} . U acts as an intermediate oxide and reduces the number of four-coordinated B, lanthanide ions serve as modifiers, with their increasing concentration shifting the B-O coordination from 3 to 4. X-ray photoelectron spectroscopy revealed a depth-dependent variation in the $\text{U}^{\text{IV}}/\text{U}^{\text{VI}}$ ratio. Leaching tests showed increased dissolution of Si, B, and Na, compared to the glass matrix.

Keywords Borosilicate glass, Neutron diffraction, Reverse monte carlo simulation, X-ray absorption spectroscopy, X-ray photoelectron spectroscopy, Leaching test

Electricity generation via nuclear energy results in the production of spent nuclear fuel (SNF). This material requires careful handling, and the proper management of the resulting waste generally involves deep geological storage within an engineered barrier system (EBS). Prior to final disposal, the SNF is reprocessed to recover valuable elements, as it still contains up to ~94% U and ~1% Pu, which can be converted into Mixed Oxides for further reuse in the nuclear fuel cycle. In the remaining elements long-lived radioactive actinides, such as Th, Np, Am and Cm can be found¹. Due to its significant radioactivity after reprocessing, it is categorized as high-level radioactive waste (HLW). Vitrification is a widely accepted method for immobilizing HLW, as the first barrier of EBS involving the encapsulation of HLW materials in a long-term, inert borosilicate glass matrix due to its excellent chemical and mechanical properties, thermal and radiation stability^{2–4}. Therefore, it is crucial to investigate the effects of radioactive chemical constituents on the structural stability and solubility characteristics of the glassy system. In our previous studies we focused on the immobilization of lanthanide rare earth elements as minor actinide surrogates due to their similar chemical properties, including comparable ionic radii^{5,6}. Ce^{III} was used to model Pu^{III} , Nd^{III} was used to model Cm^{III} , and Eu^{III} was used to model Am^{III} . The glass matrix was loaded with three different lanthanide oxides at concentrations of 10 wt% and 30 wt%. Characterization aimed to explore how the incorporation of lanthanides (Ln): Ce, Nd, and Eu ions affect the atomic properties including bond lengths and coordination environments, and fundamental structure of the glass matrix⁷. Among the non-radioactive surrogates, Ce, introduced as cerium(IV) oxide, was present in both Ce^{III} and Ce^{IV} forms, as elevated sample preparation temperatures readily reduced it to the trivalent state. In another study, we investigated a series of borosilicate model waste glasses, where the matrix glass was loaded with UO_3 at four different concentrations ranging from 10 to 40 wt%⁸. To guarantee the long-term stability of the waste glass for containment, it was important to assess its physical, chemical properties and structural characteristics.

The focus of this study is on the structural changes that occur in the borosilicate glass when loaded with mixture of lanthanides and uranium – a novel combination that has not been explored yet. The simulated waste form incorporates cerium(IV) oxide, neodymium(III) oxide, europium(III) oxide, and uranium(VI) oxide, allowing a comprehensive analysis of the combined effects of these elements, thus providing a more realistic model for nuclear waste encapsulation. Four distinct glass samples were synthesized and investigated to gain

¹Environmental Physics Department, HUN-REN Centre for Energy Research, Konkoly Thege St. 29-33, Budapest 1121, Hungary. ²HUN-REN Wigner Research Centre for Physics, Konkoly Thege St. 29-33, Budapest 1121, Hungary. ³School of Physics, Aristotle University of Thessaloniki, Thessaloniki 54124, Greece. ✉email: fabian.margit@ek.hun-ren.hu

deeper insight into the structural evolution of this complex system. The glass matrix was previously synthesized and characterized⁹. Neutron diffraction (ND) experiments, along with Reverse Monte Carlo (RMC) simulations were used to determine the structural parameters of the mixed (U, Ln) borosilicate glasses. X-ray absorption fine structure (XAFS) spectroscopy measurements were carried out at synchrotron radiation sources to better understand the local environment surrounding the three lanthanides and uranium. Given that the conditioned waste must be stored in deep underground repositories using an EBS approach, these glassy waste forms will serve as the initial containment barrier^{10,11}. The long-term chemical durability of the borosilicate model waste glass series was assessed through water alteration experiments. Leaching tests were performed with porewater in corporation with thermal analysis techniques^{12,13}. As Boda Claystone Formation (BCF) is the candidate host rock system for Hungarian HLW storage, the experiments utilized synthetic porewater formulated to replicate BCF characteristics. In addition to analyze the leachates for chemical composition, it is necessary to investigate the glass surface in contact with the liquid solution. To achieve this, we examined the glass surface using X-ray photoelectron spectroscopy (XPS).

This study investigates the structural properties of conditioned radioactive waste within a glass matrix, emphasizing how these characteristics change when incorporating both uranium and lanthanides, in contrast to matrices containing only uranium or only lanthanides, the durability of the glass matrix and the combined behavior of these elements in the matrix are also considered. A comparison of these new results with those from our previous studies and other applicable literature is discussed.

Materials and methods

Sample Preparation

The borosilicate glass system was synthesized using high-purity, analytical-grade oxide materials, including SiO_2 , Na_2O , BaO , ZrO_2 , B_2O_3 , CeO_2 , Nd_2O_3 , and Eu_2O_3 sourced from Sigma-Aldrich in Budapest, Hungary, while UO_3 was supplied by Reactivul, Bucharest, Romania. The isotopic enrichment of B_2O_3 focused on increasing the abundance of the ^{11}B isotope to limit neutron absorption from ^{10}B in natural boron. Through inductively coupled plasma mass spectrometry, the ^{11}B isotope enrichment was determined to be 99.6%¹⁴. A high-temperature electrical furnace, along with a platinum crucible, was used under atmospheric conditions for sample preparation. Glasses were synthesized by melting the homogenized powder mixtures at 1450 °C and maintaining this temperature for 2 h. The molten material was then cooled to 1200 °C and quickly quenched on a stainless-steel plate. The bulk samples were powdered to 50 μm particle size through ball-milling with zirconia balls in a Retsch MM400 Mixer Mill. The following samples were synthesized and investigated: 70 wt% [Matrix] + 20 wt% UO_3 + 10 wt% CeO_2 , 70 wt% [Matrix] + 20 wt% UO_3 + 10 wt% Nd_2O_3 , 70 wt% [Matrix] + 20 wt% UO_3 + 10 wt% Eu_2O_3 , and 60 wt% [Matrix] + 10 wt% UO_3 + 10 wt% CeO_2 + 10 wt% Nd_2O_3 + 10 wt% Eu_2O_3 , where the matrix composition was $55\text{SiO}_2 \cdot 10\text{B}_2\text{O}_3 \cdot 25\text{Na}_2\text{O} \cdot 5\text{BaO} \cdot 5\text{ZrO}_2$ (mol%), (denoted as MUCe, MUNd, MUEu and MUCNE, respectively and the composition of the matrix glass referred as REF). Glass density was determined gravimetrically at 22 ± 0.5 °C using an electronic balance with a 10^{-4} g sensitivity, with distilled water serving as the immersion medium. Each sample underwent four measurements, yielding a standard deviation of less than 0.01 g/cm³. The measured density of the glasses was 2.73 ± 0.01 g/cm³, 2.88 ± 0.01 g/cm³, 2.94 ± 0.01 g/cm³, 3.05 ± 0.01 g/cm³ and 3.18 ± 0.01 g/cm³ for REF, MUCe, MUNd, MUEu and MUCNE, respectively.

X-ray absorption fine structure

Quick X-ray absorption spectrometry (QXAS) measurements were conducted at the P65 Applied XAFS beamline of the PETRA III synchrotron radiation source (DESY, Hamburg, Germany)¹⁵. Both X-ray absorption near-edge structure (XANES) and extended X-ray absorption fine structure (EXAFS) regions were covered by energy scans using a Si(111) monochromator around the L_{III} absorption edge of Eu and a Si(311) monochromator around the K-edges of Ce and Nd. The QXAS system enables a rapid acquisition of absorption spectra with a step scan time of 0.1 s and energy step of 0.5 eV.

XAFS measurements were also conducted at the B18 XAS beamline of the Diamond Light Source (Harwell, United Kingdom)¹⁶. Spectra were acquired in QXAS mode utilizing a Si(111) monochromator around the L_{III} absorption edges, covering XANES regions of Ce, Nd and Eu and both XANES and EXAFS regions for U. The experiment employed a step scan time of 0.06 s and an energy step of 0.3 eV. XAFS spectra were collected at both beamlines in transmission mode using ionization chambers for monitoring incoming and transmitted X-ray intensities. The glass samples, pressed into 13 mm diameter pellets with polyvinylpyrrolidone as the binder, were examined. The optimal quantities used during sample preparation were calculated using the XAFSmass program¹⁷. Similarly prepared pressed pellets from UO_2 , UO_3 , CeO_2 , Nd_2O_3 , and Eu_2O_3 were measured as reference compounds. All spectra were collected in ambient conditions. Data processing, including background removal, XAFS spectra normalization and linear combination fitting (LCF) was carried out with the Athena software package¹⁸. EXAFS analysis utilized FEFF8.2 to calculate theoretical phase and amplitude functions for the scattering paths, while curve fitting was conducted in both R-space and k-space with the FEFFIT tool¹⁹.

Neutron diffraction

For the MUEu and MUCNE glassy samples, ND measurements were carried out using the PSD diffractometer ($\lambda_0 = 1.068$ Å, $Q \leq 9.8$ Å⁻¹)²⁰ at the Budapest Neutron Centre, while the MUCe and MUNd samples were measured with the 7C2 diffractometer ($\lambda_0 = 0.726$ Å, $Q \leq 15.3$ Å⁻¹)²¹ at the Laboratoire Léon Brillouin. Each powder sample, weighing about 5 g, was placed in thin-walled cylindrical vanadium sample holders with diameters of 8 mm (PSD) and 6 mm (7C2). The raw data were corrected for detector efficiency, background scattering, and absorption effects. Total structure factors were calculated using local software packages, and a detailed description of the data evaluation was provided previously⁹.

Reverse Monte Carlo simulation

The RMC simulation is a powerful method for constructing large 3D structural models compatible with experimental data, particularly $S(Q)$ diffraction structure factors²² and $\chi(k)$ EXAFS curves²³ and various physical and chemical constraints (density, minimum interatomic distances, coordination numbers, bond angle distributions or even Q^n distributions). In this paper structural models are generated by fitting neutron diffraction structure factors and EXAFS data measured at the U L_{III} -edge. Simulations are carried out by the RMC++ code²⁴. The RMC algorithm calculates the one-dimensional partial atomic pair correlation functions $g_{ij}(r)$, and then uses inverse Fourier transformation to derive the partial structure factors $S_{ij}(Q)$, as described in Eq. (1):

$$S_{ij}(Q) = 1 + \frac{4\pi\rho_0}{Q} \int r [g_{ij}(r) - 1] \sin Qr dr \quad (1)$$

where ρ_0 denotes the atomic number density. The simulation process involves adjusting the atomic positions randomly until the calculated $S(Q)$ matches the experimental data within the experimental error margin.

Using the RMC method, $g_{ij}(r)$ were obtained. The weighting factors, w_{ij} and $S_{ij}(Q)$ were defined by Eq. (2) and Eq. (3):

$$w_{ij} = \frac{c_i c_j b_i b_j}{\left[\sum_{i,j}^k c_i b_j \right]^2} \quad (2)$$

$$S(Q) = \sum_{i,j}^k w_{ij} S_{ij}(Q) \quad (3)$$

where c_i and c_j are the molar fractions of the components, b_i and b_j are the coherent neutron scattering lengths, and Q stands the momentum transfer. In the case of MUCe, MUNd and MUEu $k=8$ (number of different components in the sample) which corresponds to a total of 36 atom pairs based on $k(k+1)/2 = 36$ and in the case of MUCNE sample the total atom pairs is 55. The neutron-weighted factors for the atomic pairs with the largest contribution to the ND can be found in Table 1.

Model $\chi(k)$ EXAFS curves are obtained from the partial correlation functions by the following Eq. (2)³:

$$\chi_i(k) = \sum_j \int_0^{r_{max}} 4\pi \rho_0 c_j r^2 g_{ij}(r) B_{ij}(k, r) dr \quad (4)$$

where i denotes the absorbing component, j runs over all components, while $B_{ij}(k, r)$ is the ‘backscattering matrix’ that gives the k - and r -dependent elementary contribution of a j type neighbor to the model curve. The right hand side of Eq. (4) is the superposition of backscattering contributions from all neighboring atoms.

As backscattering of photoelectrons is strongly damped by distance, EXAFS spectra of glasses usually contain information only on the first coordination shell. (It is to be noted that for crystalline systems the contribution of further shells should often be taken into account²⁵. It was assumed that, in the glasses investigated, only oxygen atoms can be found in the first coordination shell of U atoms. Therefore, model U L_{III} EXAFS spectra depend directly only on U-O correlations. Elements of the U-O backscattering matrix were calculated by the FEFF9 code²⁶.

Starting configurations were obtained by placing 10,000 atoms randomly in cubic boxes. The sizes of the simulation boxes were chosen to comply with the experimentally determined density (see above). The RMC simulations incorporated two types of constraints: minimum interatomic distances (cut-offs) and two coordination constraints. Si-O and B-O cut-offs were 1.4 Å and 1.2 Å, respectively. Minimum metal-O distances were 1.7–1.8 Å, while all metal-metal cut-offs were 3 Å. Minimum Si-Si, Si-B and B-B distances were chosen to be 2.8 Å, 2.5 Å and 2.3 Å, respectively. The cut-off values were based on earlier results for SiO_2 - Na_2O ²⁷, B_2O_3 - Na_2O glasses²⁸, the matrix glass⁹, the matrix glass with lanthanides²⁹ and the matrix glass loaded with UO_3 ⁸.

Coordination constraints can help to reduce the uncertainty of the structural parameters deduced from RMC-generated models. In the present study the following coordination constraints were applied for all glasses investigated: (i) the Si-O coordination number was constrained to be 4 for all Si atoms, (ii) each B atom had to have at least 3 O neighbors (3 and 4 were both allowed). The above coordination constraints were satisfied usually at least by 88% and 96% of the atoms for the Si-O and B-O, respectively. In addition, the average U-O coordination number was also constrained to the values obtained by EXAFS data analysis (see below).

	Weighting factor, w_{ij} [%]									
	Si-O	B-O	Na-O	Ba-O	Zr-O	Ce-O	Nd-O	Eu-O	U-O	O-O
REF	18.68	10.32	12.24	1.58	3.68	-	-	-	-	39.95
MUCe	15.68	7.27	12.47	1.65	2.46	4.03	-	-	1.91	42.30
MUNd	15.42	7.16	12.27	1.65	2.45	-	3.96	-	3.12	41.04
MUEu	15.47	7.20	12.33	1.70	2.43	-	-	4.00	2.79	41.32
MUCNE	14.51	6.79	11.65	1.62	2.32	1.82	1.80	2.88	2.74	40.80

Table 1. Neutron-weighted factors, w_{ij} [%], for the X-O and O-O partial interatomic correlations.

X-ray photoelectron spectroscopy

XPS was used to determine sample composition at the surface and in the surface range using an ESCALAB Xi⁺ equipment from Thermo Scientific. Three positions were detected on each mm-sized glass piece. Due to the insulating nature of the samples, continuous dual charge compensation (both positive and negative) was applied to prevent electrical charge-up. However, the curvature of the glass samples caused uneven charging, leading to a widening of the detected XPS peaks. The detected peaks included the main components Si 2p (99 eV) and O 1s (532 eV), along with dopants such as B 1s (186 eV), Ba 3d (780 eV), Zr 3d (182 eV), Na 1s (1072 eV), C 1s (284 eV), Ce 3d (882 eV), Nd 3d (982 eV), Eu 3d 5/2 (1134 eV), and U 4f 7/2 (380 eV). Observations took place analyzing the sample surface in “as received” state that involves some organic contamination. Effort to remove surface contamination (e.g. Ar cluster sputtering) was not successful since the sputtering caused changes in the matrix itself too. On the MUE and MUCNE samples depth profile measurements were carried out with Ar⁺ ion sputtering to reveal the depth dependence of composition. Ion sputtering was performed using a 500 eV Ar⁺ beam at a 45° angle of incidence, scanned across a 2 mm × 2 mm area. This process removed approximately 2 nm of material per step, with a total removal of about 30 nm. The XPS spot size for measurement was 500 μm, focused at the center of the sputtered square. The measured spectra were evaluated by determining the peak intensities. A peak fitting algorithm was applied to decompose complex peak shapes and separate the Na Auger peak from the oxygen 1s peak. Component concentrations were calculated using sensitivity factors from the ALTHERMO1 library, assuming a homogeneous target.

Leaching test

The Product Consistency Test is an effective method for assessing the chemical durability of glassy wasteform systems and the alterations in their structure resulting from interactions with leaching solutions. This test provides valuable data on both the release rates of structurally immobilized uranium and actinide surrogates and the alteration in the composition of the leaching solution. According to the ASTM C1285-21 protocol³⁰ the normalized release rates and glass dissolution rates for silicate, boron, uranium, and lanthanides can be determined using Eq. (5) and Eq. (6):

$$NL_i = \frac{c_i(\text{sample})}{(f_i) \bullet \left(\frac{SA}{V}\right)} \quad (5)$$

$$NR_i = \frac{c_i(\text{sample})}{(f_i) \bullet \left(\frac{SA}{V}\right) \bullet (t)} \quad (6)$$

where c_i denotes the concentration of the element of interest in the soaking water (g/L), f_i is the weight fraction of the element in the original borosilicate glass (unitless), SA/V is the ratio of the surface area of the final waste form to the volume of the leachate (m^{-1}) and t indicates the duration of the test (days).

Since the BCF is regarded as a potential host rock system for HLW storage in Hungary, experiments were conducted using synthetic porewater designed to reflect the characteristics of the albitic claystone in BCF. The porewater chemistry was modeled using the MINSORB geochemical speciation software and the Nagra/PSI 01/01 thermodynamic database^{12,13}. The porewater composition was calculated with a fixed p_{CO_2} of $10^{-3.5}$ bar and a pH of 8.0, maintaining equilibrium with atmospheric CO_2 and saturation with calcite, dolomite, and quartz. To achieve charge neutrality, Na^+ and Cl^- concentrations were adjusted, while concentrations of Ca, Mg, Si, and C(IV) were set according to predefined conditions³¹. The composition of the resulting synthetic Boda porewater (SBPW) is given in Table 2³².

For the test method, a 100 to 200 mesh fraction of the crushed sample is used, from which the adhering fine is removed. Around 1 g of the sample is placed into cylindrical 304 L stainless steel vessel, an amount of SBPW equal to ten times the sample mass is added. The sealed system is kept in a laboratory oven at a constant temperature of 90 ± 2 °C. The surface area to volume ratio (SA/V) was determined to be 1600 m^{-1} for all samples, based on the assumption that the glass particles were cubic in shape throughout the calculations. After 3, 7, and

Element, ion	Concentration (mol/L)
Na	1.7×10^{-2}
K	1.8×10^{-4}
Mg	2.3×10^{-3}
Ca	3.1×10^{-3}
Sr	1.5×10^{-5}
Cl^-	2.3×10^{-2}
SO_4^{2-}	1.9×10^{-3}
$\text{HCO}_3^-/\text{CO}_3$	6.1×10^{-4}
Ionic strength (mol/L)	3.3×10^{-2}
pH	8.1
Eh (mV)	−300

Table 2. Chemical composition of the synthetic Boda Porewater (SBPW).

	$U^{VI}-O_{axial}$				$U^{VI}-O_{equatorial}$			U^V-O			
	$N(O)$	$U^{VI} [at\%]$ (x)	$R [\text{\AA}]$	$DW [\times 10^{-3} \text{\AA}^2]$	$N(O)$	$R [\text{\AA}]$	$DW [\times 10^{-3} \text{\AA}^2]$	$N(O)$	$U^V [at\%]$ (1-x)	$R [\text{\AA}]$	$DW [\times 10^{-3} \text{\AA}^2]$
MUCe	$2 \times x$	75 ± 6	1.85 ± 0.01	1.5	$6 \times x$	2.30 ± 0.03	14.8	$6 \times (1-x)$	25 ± 6	2.20 ± 0.02	2.4
MUNd	$2 \times x$	65 ± 8	1.83 ± 0.01	1.5	$6 \times x$	2.29 ± 0.03	13.6	$6 \times (1-x)$	35 ± 8	2.20 ± 0.02	3.1
MUEu	$2 \times x$	63 ± 6	1.85 ± 0.01	2.3	$6 \times x$	2.28 ± 0.03	13.2	$6 \times (1-x)$	37 ± 6	2.18 ± 0.02	1.7
MUCNE	$2 \times x$	73 ± 7	1.84 ± 0.01	1.4	$6 \times x$	2.28 ± 0.03	13.8	$6 \times (1-x)$	27 ± 7	2.20 ± 0.02	1.5

Table 3. Best fit parameters obtained from the U- L_{III} EXAFS fitting results of the Ln and U loaded glass samples.

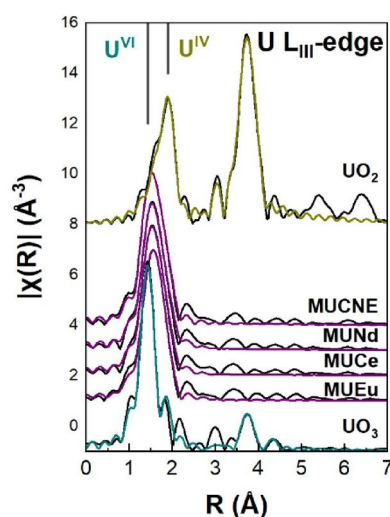


Fig. 1. Fourier transforms of the $\chi(k)$ U L_{III} EXAFS spectra for the Ln and U loaded glassy samples. The experimental data are shown in black while the fitting is depicted with the color line. The figure also includes experimental data and fitting curve of reference UO_3 and UO_2 .

10 days, the vessels were unsealed, and the leachates were passed through a $0.45 \mu\text{m}$ syringe filter. Following filtration, the leachates were acidified with concentrated HNO_3 and analyzed by inductively coupled plasma optical emission spectroscopy (ICP-OES) using a Perkin Elmer Avio 200 ICP-OES instrument.

Results and discussion

Local environments of uranium and lanthanides with EXAFS

The U L_{III} -edge EXAFS spectra were fitted assuming the presence of U^{VI} ions as uranyl in a linear arrangement with 2 O atoms ($O=U=O$) and 6 O atoms in an equatorial plane and U^V in octahedral coordination, denoted as $U^{VI}-O_{axial}$, $U^{VI}-O_{equatorial}$ and U^V-O in Table 3 respectively. In particular, the fitting of the $\chi(k)$ EXAFS spectra was performed simultaneously for all studied samples within the k -range of $3-13 \text{\AA}^{-1}$. Curve fitting was performed in the first nearest neighbor (nn) shell, with the fitting parameters including the percentage of U atoms in the two different sites, the Debye-Waller (DW) factors and the U-O bond length. The values of the amplitude reduction factor (S_0^2) and energy origin (E_0) were constrained to be equal although iterated in order to provide the best fitting results. The Fourier Transforms (FTs) of the $\chi(k)$ EXAFS spectra are presented in Fig. 1, the raw and fitted $\chi(k)$ EXAFS are shown in Figure S1(a) in the Supplementary material, while the best fit parameters are included in Table 3. Compared to the previous set of glass samples with U, a notable finding is the slight increase of the U^V-O bond length compared to the MU10-MU40 glasses⁸ by $0.05-0.07 \text{\AA}$. This change is accompanied by an increase in the static disorder of the $U^{VI}O_6$ octahedra, as the increased values of the DW factors ($\sim 15 \times 10^{-3} \text{\AA}^2$) suggest. However, the calculated U-O bond lengths are consistent with those found in comparable glassy samples^{3,33} and shows a high level of consistency with the results derived from RMC.

As it is revealed by the EXAFS analysis results, in our sample series a weak, systematic decline in the atomic percentage of hexavalent uranium in the glass can be observed when lanthanides with higher atomic numbers (Z) are used. This trend is shown in Figure S2 in Supplementary material.

Sample thickness was optimized specifically for the U L_{III} -edge, with adjustments limited by regulatory restrictions on U handling. Since optimal Ce, Nd, and Eu measurements required thicker samples, supplementary

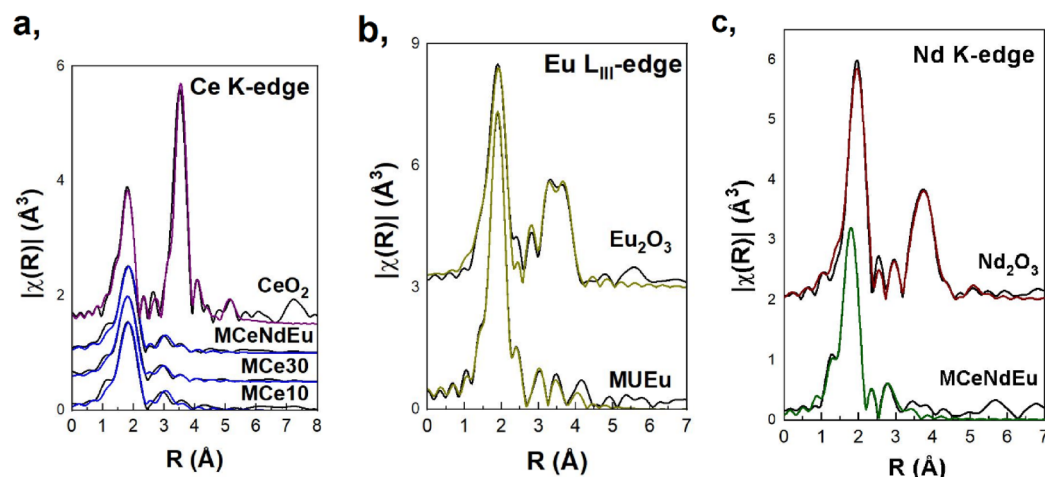


Fig. 2. Fourier Transforms of the $\chi(k)$ EXAFS spectra for the supplementary Ce loaded samples and MCEndEu recorded at the Ce K-edge (a), for the MUEu sample at the Eu L_{III} -edge (b), and for the MCEndEu sample at the Nd K-edge (c). The experimental data and fitting curve of reference CeO_2 , Eu_2O_3 and Nd_2O_3 are also included.

	$N(O)$	$R_{Ce-O} [\text{\AA}]$	$DW [\times 10^{-3} \text{\AA}^2]$	$N(Si)$	$R_{Ce-Si} [\text{\AA}]$	$DW [\times 10^{-3} \text{\AA}^2]$
MCE10	6.0 ± 0.4	2.44 ± 0.01	14.9	1.5 ± 0.3	3.67 ± 0.02	8.2
MCE30	5.9 ± 0.3	2.42 ± 0.01	15.7	0.9 ± 0.2	3.64 ± 0.02	5.7
MCEndEu	5.5 ± 0.6	2.44 ± 0.01	13.8	1.0 ± 0.2	3.67 ± 0.02	4.2
CeO_2	8	2.35 ± 0.01	12	12 (Ce)	3.85 ± 0.02	4.3

Table 4. Best fit parameters obtained from the Ce-K EXAFS results of the Ln loaded glassy samples. Values in bold were kept fixed throughout the fitting process.

samples without U were prepared at these increased thicknesses for optimal EXAFS data acquisition including one sample containing all relevant lanthanides: 70 wt% [Matrix] + 10 wt% CeO_2 + 10 wt% Nd_2O_3 + 10 wt% Eu_2O_3 (MCEndEu) and two others with CeO_2 added at different concentrations: 90 wt% [Matrix] + 10 wt% CeO_2 (MCE10) and 70 wt% [Matrix] + 30 wt% CeO_2 (MCE30). These CeO_2 loaded samples are directly comparable to those used in our previous study⁷.

The Ce K-edge EXAFS spectra of the MCE10, MCE30 and MCEndEu glasses were fitted assuming that Ce atoms form octahedra which link to SiO_4 polyhedra in the matrix. Curve fitting proceeded in the two nn shell (k -range: 3–11.5 \AA^{-1}) and the fitting parameters were the coordination numbers, DW factors and atomic distances in all shells. The values of the S_0^2 and E_0 were constrained to be equal although iterated. The FTs of the experimental data and the fitting are shown in Fig. 2(a). The respective raw and fitted $\chi(k)$ EXAFS are shown in Figure S1(b) in the Supplementary material. The fitting results, listed in Table 4, indicate the presence of Ce in octahedral coordination. These results are in good agreement with the RMC calculations according to which the O atoms are expected at a distance of 2.55 \AA from the Ce atoms²⁹. Furthermore, both the coordination number and Ce–O bond length suggest the network forming role of Ce, contrary to CeO_2 -silicate glasses where Ce acts as a glass former³⁴. Additionally, the Ce–O bond length is much longer than the respective in the Ce^{IV} reference oxide, an indication of a change in the valence state of Ce (reduction of Ce^{IV})³⁵.

The Eu L_{III} -edge spectrum of the U-rich sample MUEu was fitted assuming a mixed bonding environment of Eu in the borosilicate glass as shown in Fig. 2(b). The fitting of the $\chi(k)$ EXAFS spectra (as shown in Figure S1(c) in the Supplementary material) was performed in the k -range of 2.8–12.0 \AA^{-1} in the two nn shells. The model used for the fitting assumes that a fraction x of Eu atoms is 10-fold coordinated with O atoms, surrounded by BO_4 tetrahedra, based on the crystalline structure of LaB_3O_6 , where La has been substituted with Eu³⁶. The remaining $y = 100 - x$ Eu atoms form pentagonal bipyramids EuO_7 that connect via corners to SiO_4 units³⁷. The fitting parameters were the percentage of the Eu in the two distinct sites, the DW factors and the atomic distances in all shells and also the value of the E_0 . The value of the S_0^2 was kept fixed to the respective value derived from the analysis of the reference Eu_2O_3 ($S_0^2 = 0.9$). The best fit parameters are presented in Table 5.

No major changes were detected in the bonding environment of Eu as a result of U-incorporation, a finding that confirms that Eu acts as a typical network modifier, as previously revealed in the Matrix–Eu glasses⁷.

As in the case of Eu-glass, the Nd K-edge spectrum of the U-free glass MCEndEu was fitted assuming a mixed bonding environment of Nd in the borosilicate glasses as presented in Fig. 2(c). The fitting of the $\chi(k)$ EXAFS spectrum (shown in Figure S1(d) in the Supplementary material) was performed in the k -range of 3.0–11.0 \AA^{-1} in the two nn shells. In particular, it was assumed that a fraction x of Nd atoms is 10-fold coordinated to O and

Eu L _{III} -edge			
	N	R [Å]	DW [$\times 10^{-3}$ Å ²]
MUEu		$x = 79 \pm 8$ [at%]	
O	10 $\times x$	2.41 ± 0.01	21.4
B	10 $\times x$	3.37 ± 0.02	1.6
O	7 $\times (1-x)$	2.34 ± 0.03	19.9
Si	4 $\times (1-x)$	3.57 ± 0.04	7.1
Eu ₂ O ₃			
O	6	2.37 ± 0.01	10.8
Eu	6	2.64 ± 0.02	8.5
Eu	6	3.82 ± 0.03	13.0
O	8	4.30 ± 0.04	5.8

Table 5. Structural parameters obtained from the Eu L_{III} EXAFS fitting results of the glassy samples. Values in bold were kept fixed throughout the fitting process.

Nd K-edge			
	N	R [Å]	DW [$\times 10^{-3}$ Å ²]
MCeNdEu		$x = 76 \pm 4.0$ [at%]	
O	10 $\times x$	2.41 ± 0.01	11.8
B	10 $\times x$	3.38 ± 0.02	17.2
O	8 $\times (1-x)$	2.35 ± 0.03	3.3
Si	6 $\times (1-x)$	3.58 ± 0.04	6.3
Nd ₂ O ₃			
O	4	2.40 ± 0.01	2.7
O	4	2.59 ± 0.02	2.8
Nd	6	3.67 ± 0.03	22.1
Nd	6	3.80 ± 0.04	9.8
O	12	4.45 ± 0.05	2.2
O	9	5.28 ± 0.06	16.3
Nd	6	5.33 ± 0.07	13.5

Table 6. Best fit parameters obtained from the analysis of the Nd-Kedge EXAFS spectra. Values in bold were kept fixed throughout the fitting process.

links to borate chains made up from $[\text{B}_6\text{O}_{12}]^{6-}$ structural units (the crystalline structure of EuB_3O_6 was used, where Eu has been substituted with Nd)³⁸. The remaining $y = 100 - x$ Nd atoms is 8-fold coordinated and link to SiO_4 units³⁹. The fitting parameters were the percentage of Nd in the two distinct sites, the DW factors and the atomic distances in all shells and also the value of the E_0 . The value of the S_0^2 was kept fixed to the respective value derived by the analysis of the reference Nd_2O_3 ($S_0^2 = 0.97$). The corresponding fitting results are presented in Table 6.

The fitting results are similar to the previously reported results on the MNd10 and MNd30 glasses. The environment of Nd is mainly borate, yet, both the B and Si atoms are located at a longer distance from Nd, i.e. approximately by 0.2 Å. Thus, the presence of U and Ce and Eu does not have any influence on the structural role of Nd in the glasses.

Oxidation States of uranium and lanthanides with XANES

The normalized XANES spectra collected at Ln and U L_{III}-edges for glass samples and reference compounds are shown in Fig. 3. Based on our previous measurement results²⁹ Ce is the only lanthanide expected to exhibit both III and IV oxidation states. During the glass synthesis, Ce was introduced into the system as CeO_2 . However, due to the high temperature during melt quenching, partial reduction of Ce^{IV} occurred. To determine the oxidation state of Ce, the normalized XANES spectra at the Ce L_{III}-edge were compared to two reference spectra: CeO_2 for the IV oxidation state and CeTiO_3 for the III oxidation state. The results obtained from linear combination fitting (LCF) indicates that the experimental glass spectra align well with the Ce^{III} reference spectrum, which suggest an almost complete reduction of Ce in the glass samples, these results correlate well with those reported in⁵.

It was observed that the solubility of Ce in borosilicate glasses increases with temperature. At 1400 °C, the $\text{Ce}^{\text{III}}/\text{Ce}_{\text{total}}$ fraction reaches 0.9, indicating that Ce is almost completely reduced during the glass synthesis. In the MUCe sample, LCF analysis indicated 3.9% Ce^{IV} content, while in the MUCNE sample, 12.3% of Ce^{IV} was detected. These results were achieved with 10 wt% CeO_2 loading, and it is suggested that the solubility could be increased to 13 wt% due to the reduction of Ce during the process⁵. This ratio obtained is higher than that

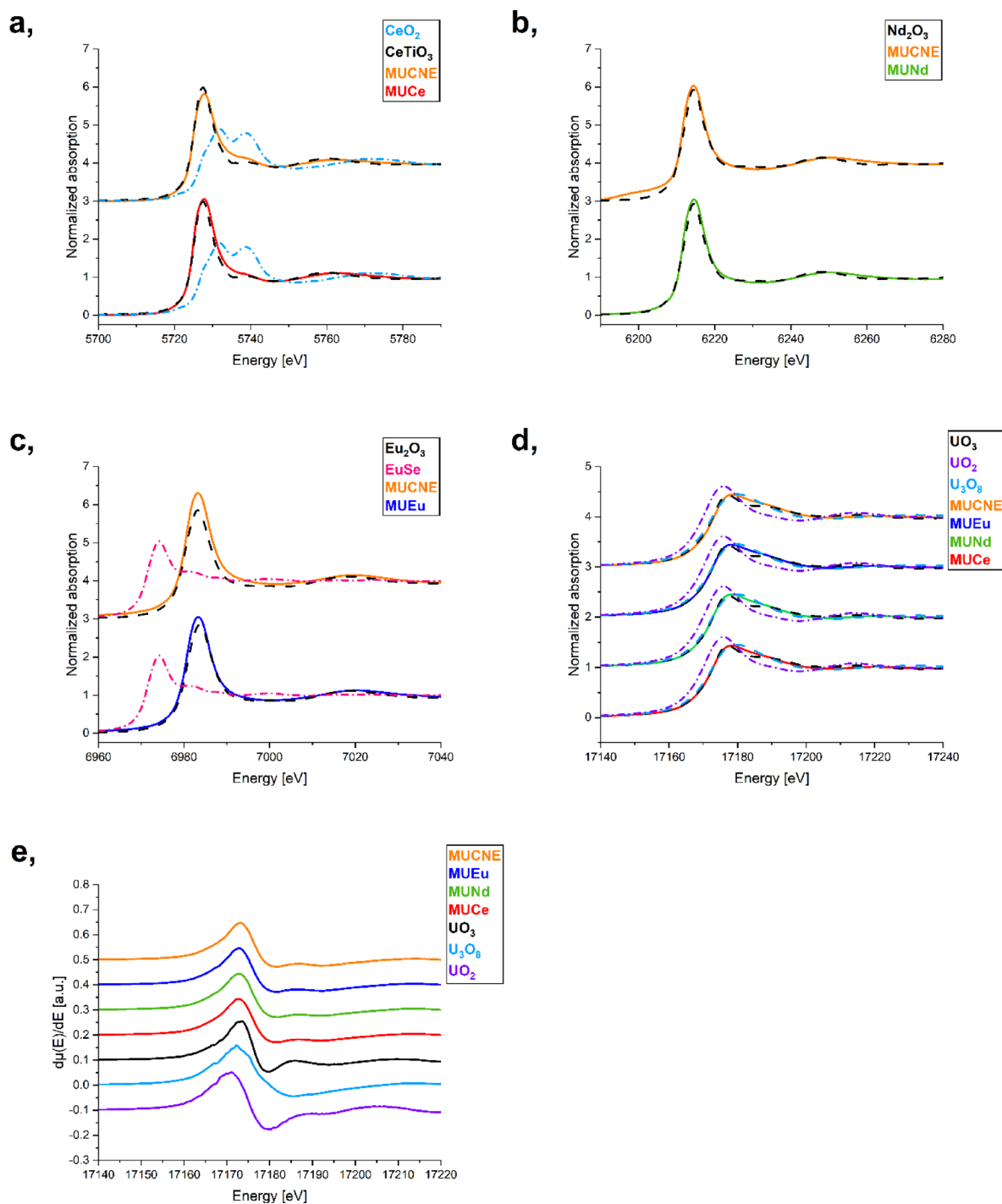


Fig. 3. Ce L_{III} (a), Nd L_{III} (b), Eu L_{III} (c), and U L_{III} (d) XANES spectra of the glassy specimens compared to the XANES spectra of the reference compounds. The solid lines represent the spectra of the U and Ln loaded glass samples, while the dashed lines represent the spectra of the references. Additionally, the first derivatives of the normalized XANES spectra (e) collected in transmission mode for the U-loaded samples and reference compounds.

achieved in our previous study, where only CeO₂ was used for loading at varying concentrations²⁹. As reported in literature⁴⁰ Nd is well soluble in glass at concentrations below 4 mol%, resulting in an amorphous glassy system. In both the MUNd and MUCNE samples, Nd was found exclusively in the III oxidation state. The same observation applies to samples containing Eu, where both samples contain only Eu^{III} ions, despite the known redox sensitivity of europium. According to the findings of Cicconi, the Eu XANES spectra exhibit systematic variations with changes in glass composition⁴¹. For Eu doped granitic and basaltic silicate glasses, the Eu^{II}/Eu_{total} molar ratio ranges from less than 1–22%, depending on the specific composition. In contrast, our previous

analysis of the Eu loaded borosilicate glass indicate that Eu^{II} comprises less than 1% of the total Eu⁷. In the current U-containing samples, no Eu^{II} contribution was identified by LCF. However, considering the already very low proportion of Eu^{II} in the U-free glass, this absence is likely due to the limitations of the LCF method, rather than a specific effect of U. Reference spectra of Eu_2O_3 and EuSe were used for Eu^{III} and Eu^{II} , respectively, in the LCF analysis.

During the analysis of the L_{III} -edge spectra, and based on our prior results, we assumed that uranium introduced as U^{VI} may undergo reduction and be present in the U^{V} oxidation state, with the potential for U^{IV} as well. Accordingly, reference spectra for UO_3 , UO_2 , and U_3O_8 were used in LCF. The analysis revealed no indication of U^{IV} , with the samples consistently showing the presence of U^{VI} and U^{V} in similar proportions, as detailed in Table 7. The partial reduction of uranium from U^{VI} to U^{V} can be explained by the high melting temperature used during glass preparation. It is known that elevated temperatures (1100–1450 °C) can shift the redox balance and lead to the formation of reduced uranium species, even without added reductants^{3,42}. The presence of U^{V} is consistent with these conditions.

The results align closely with those reported in literature^{33,43} where typical ratios of 70% U^{VI} and 30% U^{V} were also observed. When compared to earlier samples loaded solely with U, it can be concluded that the presence of lanthanides does not influence the oxidation state of U⁸.

Atomic structure from ND and U L_{III} -edge EXAFS data via reverse Monte Carlo simulation

Figure 4 presents the structure factors, $S(Q)$ obtained from ND experiments alongside the $S(Q)$ functions derived from RMC simulations.

The ND patterns reveal that the samples were fully amorphous, indicating that the implemented quenching was sufficient to ensure vitrification. The RMC calculations show excellent convergence, with the final simulated $S(Q)$ closely matching the experimental data. Additionally, the ND experimental curves are quite similar across all samples, with only minor differences observed in the low Q -range around 1.4–2.0 \AA^{-1} and between 9.0 and 10.0 \AA^{-1} . The basic structure of the (U, Ln) mixed glass remained highly similar to the REF glass, the peaks are observed at 2.9–3.0 \AA^{-1} and 5.4–5.5 \AA^{-1} . Utilizing the RMC++ code, partial atomic pair correlation functions and their coordination numbers were generated. In principle, information on the coordination environments of the components can be obtained from the partial pair distribution functions produced by the RMC calculations. It should be noted, however, that due to the limitations of the experimental data and RMC the separation of all 36 partial pair correlation functions of an eight-component glass is not realistic and therefore beyond the scope of the present study. Therefore, we concentrate on the partial correlations that either have a large weight in the neutron diffraction or EXAFS datasets (Si-O, B-O, O-O, U-O) or pinned by the constraints applied (Si-Si). The corresponding distances including the second neighbor Si-Si and Si-B distances are shown in Table 8, while the coordination numbers are given in Table 9.

The Si-O interatomic distance was obtained around 1.60 ± 0.02 \AA across all compositions as shown in Fig. 5.

This value is close to the Si-O bond length of the REF glass and also agrees with the literature, where rare earth metals are similarly used as loading ions^{44,45}. In contrast, a study involving trivalent lanthanide ions, where sodium silicate glass was loaded with 6 mol% La_2O_3 and Dy_2O_3 , reported bond distances that were 0.04 \AA longer⁴⁶. The values for the Si-O coordination number, determined under the specified constraints, are presented in Table 9.

Due to the Si-O coordination constraints the vast majority of Si atoms are surrounded by 4 O neighbors. A consequence of the presence of well-defined SiO_4 units is that the first peak of $g_{\text{SiSi}}(r)$ is also well defined. However, a slight deviation from the ideal configuration is noted. The Si-O coordination numbers remain highly similar regarding the MUCe, MUNd and MUCNE samples, while MUEu has the lowest value. A loading of 10 wt% Eu_2O_3 with the combination of 20 wt% UO_3 resulted in a higher concentration of non-bridging oxygen compared to the reference sample. In contrast, the 5.42 wt% Eu_2O_3 loading in the glass sample labeled as CJ₁-Eu, as reported in⁴⁷ did not yield the same increase in non-bridging oxygen. The presence of Ce^{III} and Nd^{III} ions results in the same decrease in the number of non-bridging oxygen atoms, as indicated by the increase in the coordination number compared to the REF glass.

A notable similarity in Si-Si first neighbor distances is observed across the sample series and a small increase is noted relative to the REF glass. For the MUCe and MUNd samples, a value of 3.10 ± 0.05 \AA is observed, whereas a slightly lower values of 3.06 ± 0.05 \AA and 3.07 ± 0.05 \AA are obtained for the MUEu and MUCNE samples. The interatomic distances are somewhat shorter than in the L_2O_3 - Na_2O - SiO_2 glass⁴⁸ and are in good agreement with the values measured in the vitreous SiO_2 , and 70 SiO_2 -30 Na_2O glasses^{27,49}. Compact SiO_4 units appear to form in the glass structure, as suggested by both the interatomic distances and coordination numbers.

	U^{VI} [%]	U^{V} [%]
MUCe	68 ± 2	32 ± 2
MUNd	65 ± 2	35 ± 2
MUEu	65 ± 2	35 ± 2
MUCNE	68 ± 3	32 ± 3

Table 7. Ratio of U^{VI} to U^{V} in the samples determined with LCF fitting, using UO_3 as the reference for U^{VI} , UO_2 for U^{IV} , and $\text{U}^{\text{VI}}\text{U}^{\text{V}}_2\text{O}_8$ for a mixture of 1/3 U^{VI} and 2/3 U^{V} . The fitting range was set between –20 and 70 eV from the absorption edge energy⁴³.

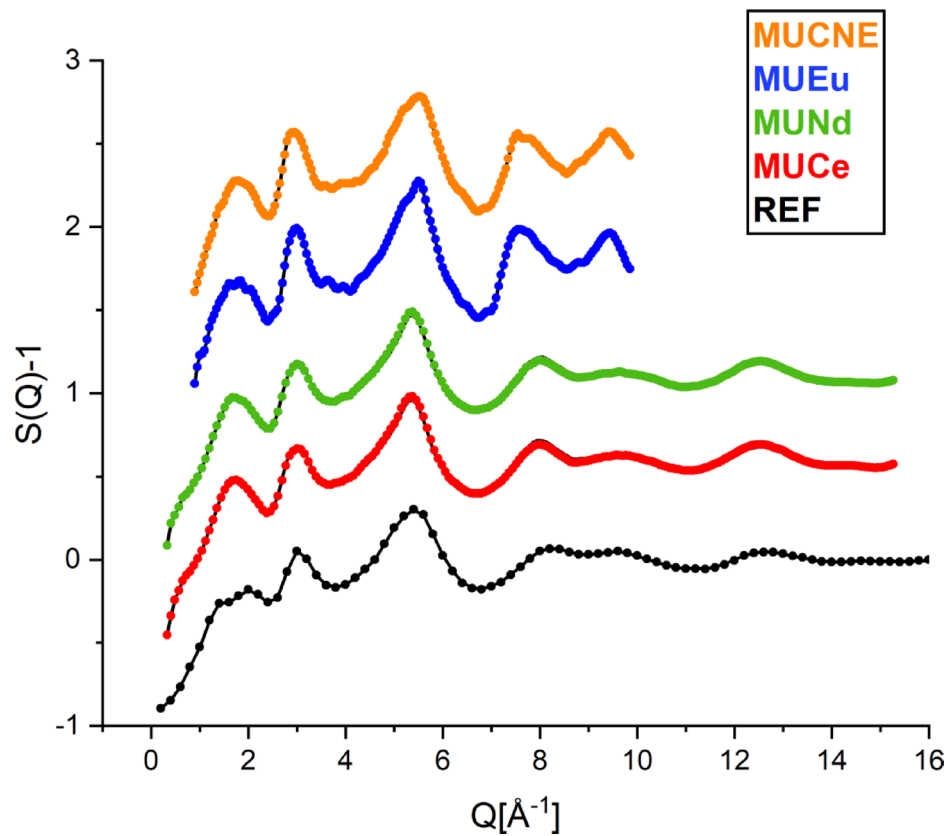


Fig. 4. Total structure factors derived from ND on REF (black circles (7C2)), MUCe (red circles (7C2)), MUNd (green circles (7C2)), MUEu (blue circles (PSD)) and MUCNE (orange circles (PSD)), each data set is accompanied with the respective RMC fit curves (black solid lines).

	Interatomic distances, r_{ij} [Å]				
	Si-O	B-O	U-O	Si-Si	Si-B
REF ⁹	1.60 ± 0.005	$1.40/1.60 \pm 0.01$	-	3.00 ± 0.1	$2.5-3.1 (\pm 0.1)$
MUCe	1.60 ± 0.02	$1.34/1.59 \pm 0.03$	$1.83/2.31 \pm 0.02$	3.10 ± 0.05	2.89 ± 0.05
MUNd	1.60 ± 0.02	$1.33/1.59 \pm 0.03$	$1.83/2.30 \pm 0.02$	3.10 ± 0.05	2.91 ± 0.05
MUEu	1.60 ± 0.02	1.54 ± 0.04	$1.83/2.31 \pm 0.02$	3.06 ± 0.05	2.91 ± 0.05
MUCNE	1.60 ± 0.02	1.52 ± 0.04	$1.83/2.32 \pm 0.02$	3.07 ± 0.05	2.85 ± 0.05

Table 8. Interatomic distances, r_{ij} [Å] obtained from the RMC simulations. Based on the reproducibility of the RMC runs, the estimated errors are also given.

	Coordination number, CN _{ij}				
	Si-O ($r_1:1.30-r_2:1.90$)	B-O ($r_1:1.20-r_2:1.75$)	U-O ($r_1:1.60-r_2:2.70$)	Si-Si ($r_1:2.80-r_2:3.40$)	Si-B ($r_1:2.50-r_2:3.40$)
REF ⁹	3.70 ± 0.02	3.05 ± 0.02	-	-	-
MUCe	3.87	3.40 ± 0.03	6.60	1.72 ± 0.1	0.66 ± 0.02
MUNd	3.86	3.51 ± 0.03	6.19	1.79 ± 0.1	0.67 ± 0.02
MUEu	3.63	3.25 ± 0.02	6.60	1.65 ± 0.5	0.64 ± 0.02
MUCNE	3.84	3.47 ± 0.03	6.54	1.61 ± 0.5	0.61 ± 0.02

Table 9. Average coordination numbers, CN_{ij}, determined from RMC simulations for Si-O, B-O, U-O and Ln-O atomic pairs, with parentheses showing the range used for the calculation of the coordination values. Constrained values are given in bold.

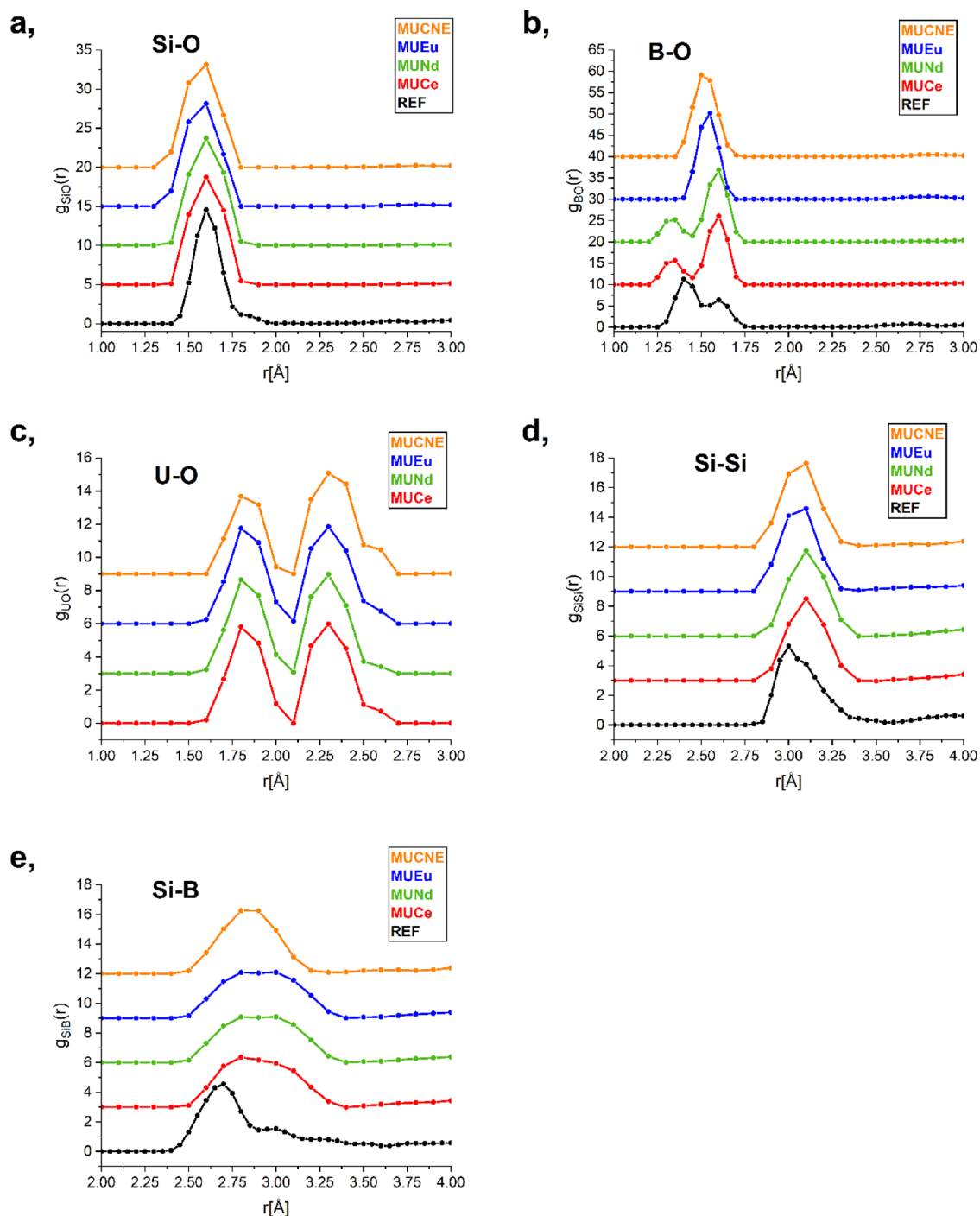


Fig. 5. Partial atomic pair correlation functions for Si-O (a), B-O (b), U-O (c), Si-Si (d), and Si-B (e) with the curves vertically shifted along the Y-axis for clarity.

Regarding the B-O network, where the working wavelength of 0.726 \AA allowed a Q -range extending to 15.3 \AA^{-1} , two interatomic distances revealed two distinct peaks with a notable decreasing trend for the first peak as shown in Table 8; Fig. 5. In contrast, the MUEu and MUCNE samples exhibited a broader distribution with a single peak. This is due to the medium Q -range in the neutron diffraction measurements ($0.45\text{--}9.8 \text{ \AA}^{-1}$), thus the limited resolution of the PSD instrument the B-O peaks for MUEu and MUCNE are not resolved and have a non physical split shape. Our previous studies indicate that the intensity of the peak at a shorter distance ($\sim 1.35 \text{ \AA}$) increases when Ln ions are incorporated into the glass structure. There is no significant difference in peak intensities between Ce, Nd, and Eu loading²⁹. However, concerning U loading, we observed that increasing the UO_3 content affects the relative intensities of the two peaks. As the UO_3 content increases, the intensity of the first peak increases, and by 40 wt%, it surpasses the peak at 1.60 \AA ⁸. As a result, the peak symmetry for MUCe

and MUND samples are identical due to the equal Ln and U content. The broader peak positions for the MUEu and MUCNE samples show strong agreement, although the measured bond lengths are slightly longer than those reported in^{47,50}. For a more detailed understanding of the B-O connections, a coordination number distribution analysis was carried out, as the ratio of BO_3 and BO_4 units is crucial for the formation of the basic matrix glass structure. Uranium trioxide and Ln oxides behave differently: while the addition of U leads to a decrease in four-coordinated B, acting as an intermediate oxide according to literature^{8,51} Ln ions act as modifiers^{47,52,53}. As their concentration increases, the B-O coordination number shifts from 3 to 4. This is reflected in the increase in coordination number, attributed to the higher number of $[\text{BO}_4]^-$ units, thus reducing the non-bridging oxygens and promoting isomerization: $\text{BO}_3 + \text{O}^- \rightarrow [\text{BO}_4]^-$. These results are consistent with our previous study⁷ showing that when the same amounts of Ln ions are incorporated into the basic glass structure, the coordination numbers remain quite similar.

The Si-B correlation is observed over a broad range between 2.4 ± 0.05 Å and 3.4 ± 0.05 Å, indicating an interaction between Si-centered and B-centered groups^{54,55}. These results suggest that the short-range order is composed of correlating tetrahedral SiO_4 , trigonal BO_3 , and tetrahedral BO_4 units, which establish a basic network structure through mixed $^4\text{Si-O-}^3\text{B}$ and $^4\text{Si-O-}^4\text{B}$ linkages^{54,56}.

The U-O partial atomic pair correlation functions show two characteristic distances at about 1.83 ± 0.02 Å and 2.30 ± 0.04 Å in all samples as shown in Fig. 5; Table 8. Furthermore, the fitting of the EXAFS data used for the U-O partial pair correlation function in both k-space and r-space is presented in Fig. 6.

These values are consistent with earlier findings in a glass containing 30 wt% UO_3 ⁸. The results of the RMC simulation are also consistent with the direct analysis of the U L_{III} EXAFS spectra (see below). The average U-O coordination numbers corresponding to the shorter and longer U-O distances are ~ 2 and ~ 4 , respectively. It is reasonable to assume that the shorter distance belongs to axially positioned O atoms, while the O neighbors at around 2.29 Å are in an equatorial arrangement^{3,57–59}. We note here that curve fitting and RMC modeling give remarkably similar results: there is a shorter U-O peak at ~ 1.83 Å and a longer, composite peak with a center of mass close to 2.3 Å. Though EXAFS spectra themselves do not clarify the very nature of this composite peak, XANES analyses reveal that it consists of $\text{U}^{\text{VI}}\text{-O}_{\text{equatorial}}$ and $\text{U}^{\text{V}}\text{-O}$ distances.

X-ray photoelectron spectroscopy of the loaded glass surfaces

XPS spectra for all elements were generally well detected, with the exception of Nd. Unfortunately, the highest intensity Nd 3d peaks are located near the O Auger peaks, specifically in the region where O loss peaks are prominent as shown in Figure S3 in Supplementary material. Due to the high O content in these glass materials, which produces strong and significant loss peaks, the low concentration of Nd could not be detected in this region. Additional attempts to detect Nd using the Nd 4d peak (120 eV) and Nd 3p peak (1298 eV) were also proved unsuccessful due to their lower intensities. One of the XPS spectra of sample MUCNE are shown below in Fig. 7. The detected peaks are decomposed into sub-components where it is meaningful. For oxygen, the metallic oxides (green on the graph) can be distinguished from the non-metallic oxides (blue on the graph), such as SiO_2 . Additionally, a Na Auger peak is visible near the O peak (turquoise on the graph). As for U, the 4f 7/2 peak presents a double peak structure, reflecting the separation between U^{IV} (green) and U^{VI} (blue) and also including an intermediate state U^{V} (turquoise) between them.

The calculated surface concentrations are averaged over the three positions and the average values are shown in Table 10. All details are provided in Table S1 in Supplementary material.

The decomposition of the O peak is uncertain, given the small energy difference (1.6 eV) between metallic and non-metallic oxides, which is smaller than the own width of components (2 eV), so O subcomponents were not detailed in Table 10. However, the decomposition of U 4f peak is reliable since the splitting of U^{IV} and U^{VI} components is high enough (3.4 eV). The total O values carry some error, as surface contamination caused over-detection by approximately 10% on original surfaces. The Eu 3d 5/2 peak was only partially detected, the total quantity was estimated by extrapolation, thus making it less precise. Eu is present in the Eu^{III} state, consistent with the normalized XANES spectra results. Ce in the Ce^{III} state, U in mixed U^{IV} , U^{V} and U^{VI} states, however, these results differ slightly from those obtained from the XANES results. In the case of Ce, the ultra-high vacuum conditions during the XPS measurements, combined with X-ray radiation, significantly promote its reduction, leading to an overestimation of the Ce^{III} concentration. This effect is particularly pronounced in the Ce 3d peaks, which explains why the lower Ce^{IV} ratio observed in the XANES results cannot be reproduced in XPS measurements^{60,61}. A similar effect is observed for U, which explains the detection of U^{IV} in small concentrations⁶². B is present as B^{III} , and Zr as Zr^{IV} . The U^{V} fraction of U in case of MUEu is not available, as the U peak is too small and noisy to allow for precise decomposition. While U is detected at very low concentrations (~ 0.1 at%), this should not be interpreted as an absence of U^{V} , but rather as a limitation in decomposition reliability at this concentration⁶³. For samples MUEu and MUCNE, the depth distributions were measured, the latter is shown in Fig. 8.

The concentration dependence show rather stable values with little alteration with depth. There is some B segregation to surface which results in B decreasing with depth. The concentrations of dopants such as Zr, Ce and Ba are weakened at the surface and, thus, increase as depth increases. The $\text{U}^{\text{IV}}/\text{U}^{\text{VI}}$ ratio appears to follow a distinctive profile, overall, the total amount of U seems to rise with depth. A similar trend was reported by Praveena et al., who observed a decreasing contribution of U^{IV} relative to U^{VI} with increasing uranium loading in borosilicate glass matrices³³. In this study, U^{IV} was clearly present at 2 mol% UO_3 , but its proportion diminished at 4 and 6 mol% loadings. In our sample, which contains approximately 3.4 mol% UO_3 , the $\text{U}^{\text{IV}}/\text{U}^{\text{VI}}$ ratio also appears to vary with depth, suggesting that both uranium content and local conditions influence the oxidation state distribution.

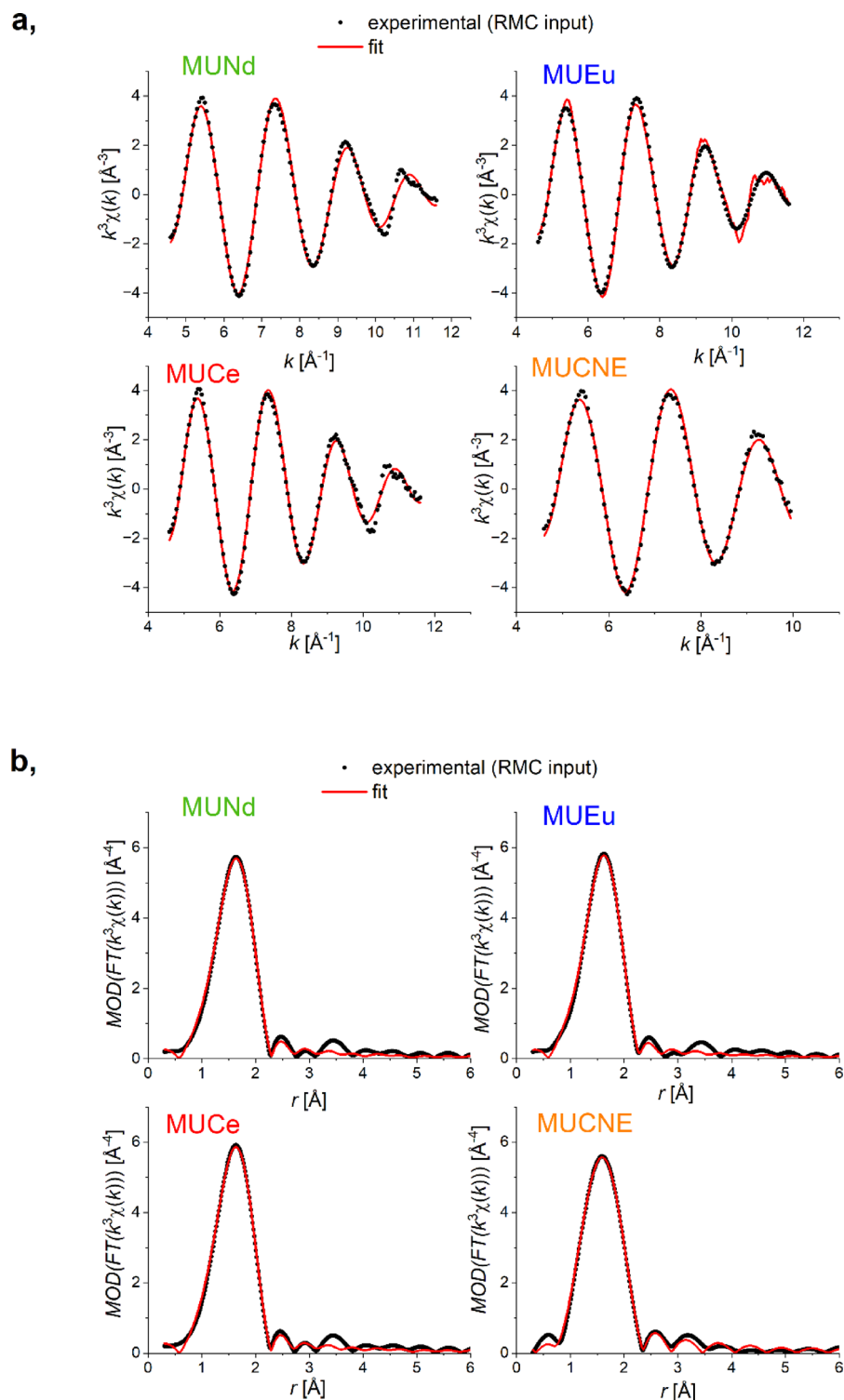


Fig. 6. EXAFS data fitting for the U-O partial pair correlation function using the U L_{III} -edge: fitting in k-space (a) and fitting in r-space (b).

Leaching test results

Composition of the leachates obtained by ICP-OES, together with the results for the REF glass and the initial SBPW solution are provided in Table 11.

In comparison to the initial SBPW solution, elevated concentrations of Si, B, and Na were observed across all samples, which can be attributed to glass dissolution. For each sample, these measured values increased over time, with the highest concentrations found in the MUNd sample. By the 10th day, the MUCe and MUNd samples showed Si and B values that were an order of magnitude higher than those of the REF-10D sample.

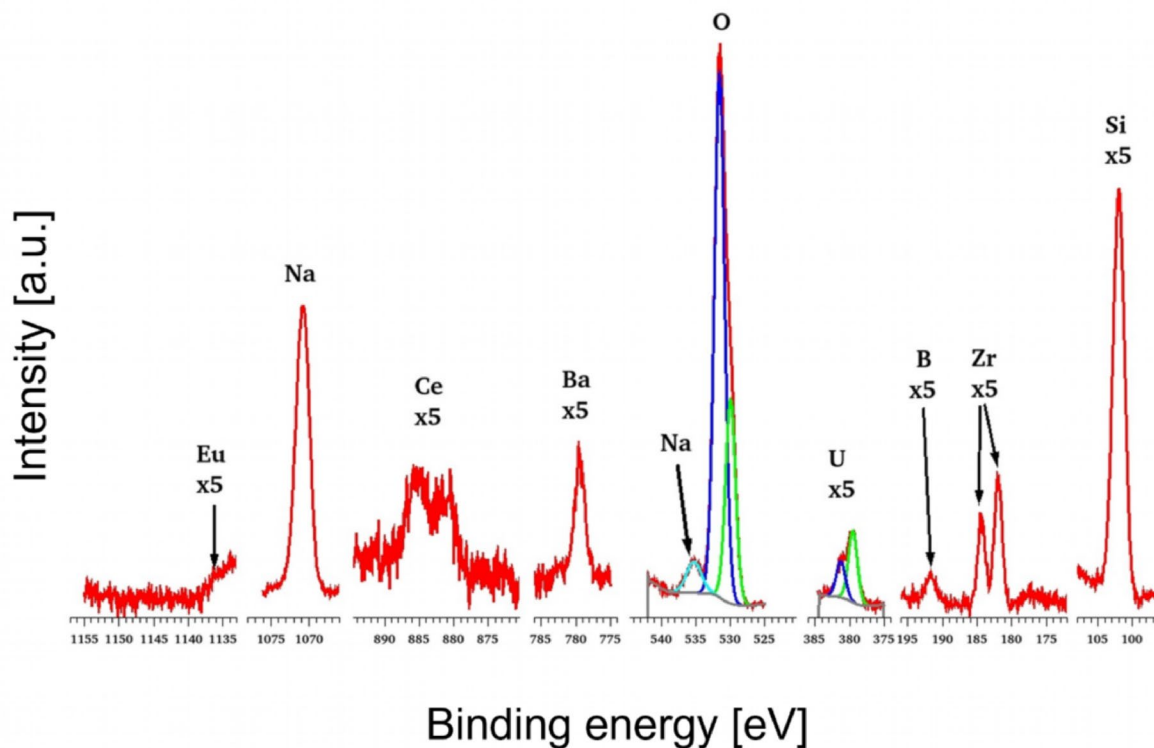


Fig. 7. XPS spectrum of sample MUCNE, the carbon peak is omitted since it is not part of the basic glass structure and Nd is also excluded due to the challenges presented by oxygen loss peak.

	Average surface concentrations [at%]											
	Si	Na	O	Zr	B	U ^{IV}	U ^V	U ^{VI}	Ba	Ce	Eu	Nd
MUCe	20.4	14.6	61.2	0.4	2.9	0.08	0.03	0.12	0.18	0.11		n.d.
MUNd	15.5	11.9	70.9	0.1	1.4	0.05	0.03	0.05	0.07			n.d.
MUEu	19.9	12.2	61.4	0.6	5.6	0.06		0.11	0.11		0.1	n.d.
MUCNE	22.0	9.4	63.6	0.8	3.4	0.03	0.05	0.06	0.22	0.39	0.1	n.d.

Table 10. Average surface concentrations for the glassy samples obtained by XPS. Nd is not determined due to measurement limitations as discussed in the text.

Although the concentration of Na remained within the same order of magnitude, it was at least twice as high in all samples. In the case of MUCNE, significantly lower concentrations were measured compared to the REF glass, not only on the final day but also at every sampling time, with Si, B, and Na levels consistently lower than those in the REF glass. The concentration of Ba decreases over time, a noticeable drop is observed by day 10 in both MUCe and MUEu samples, the Zr component of the basic glass is below the detection limit in the leachates. (The estimated detection limit of ICP-OES is 0.0007 mg/L in axial view.) Table 12 contains the normalized concentrations, mass loss, and glass dissolution rates for Si, B, U, Ce, Nd, and Eu in the lanthanide and uranium loaded borosilicate glass samples. During the PCT test, a stable borosilicate glass system is expected to keep the normalized release of glass forming elements such as Si and B below 2 g/m²/day, which was achieved by all the samples in the series³⁰. Given its high solubility in aqueous solutions, B serves as an excellent marker for assessing the glass reaction with the leaching solution. For the MUCe, MUNd, and MUEu samples, an increasing trend in the NR values for boron is observed over time, with consistently higher values at each point compared to the REF glass. Compared to our previous work on the REF glass loaded with varying content of UO₃, notable differences can be observed. When only U is incorporated into the system, the average glass dissolution rate is in the range of hundredths. However, with the presence of both U and Ln, the dissolution rate typically increases to the range of tenth⁸. A notable difference is the increasing trend in NR values. Typically, dissolution is reduced by the formation of a surface layer that prevents further glass degradation^{64,65}. This phenomenon was observed in both Ln and U loaded glass matrices. However, when both elements are present at the same time, this layer did not form within the experiment's time frame. Based on our previous measurements, the combined presence of U and Ln seems to weaken the glass structure. A decreasing trend was evident within 10 days for samples

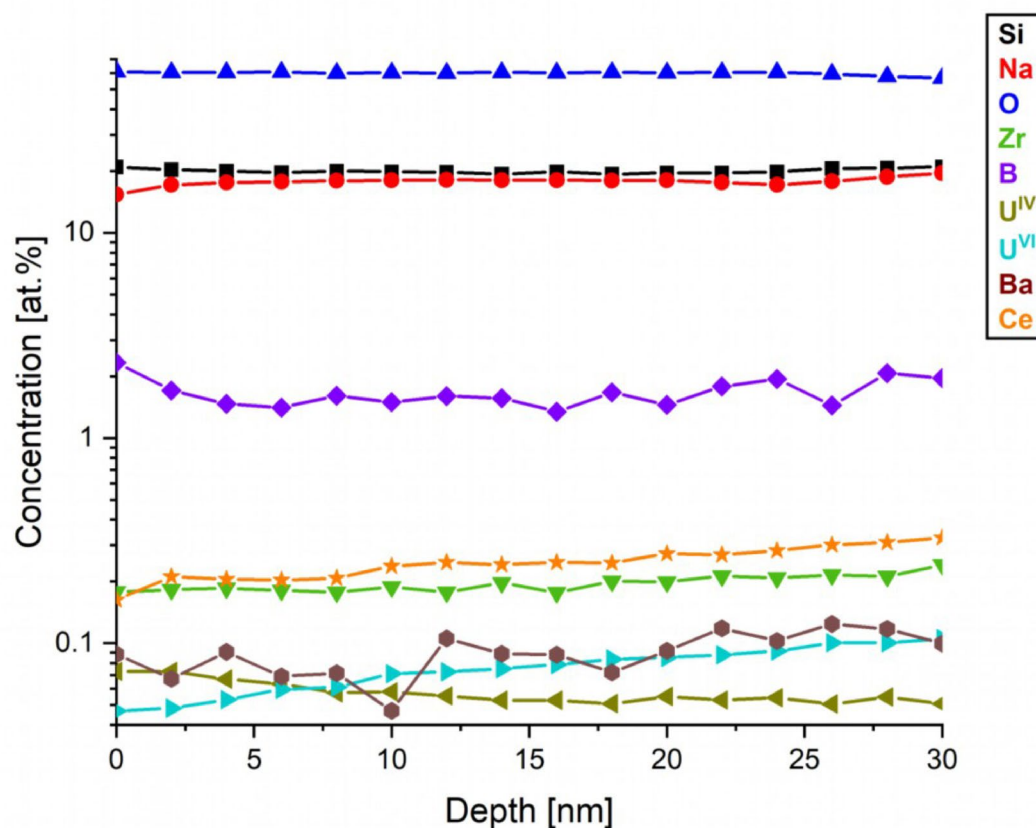


Fig. 8. XPS depth profile of the MUCNE sample surface. For the visibility of low concentration components, the concentration axis is shown in logarithmic scale.

	Concentration, c_i [mg/L]							
	Si	B	Na	Ba	U	Ce	Nd	Eu
SBPW	5.90	0.120	492	-	-	-	-	-
					-	-	-	-
REF-3D	152	44.5	780	0.501	-	-	-	-
REF-7D	335	76.9	990	0.587	-	-	-	-
REF-10D	397	82.3	1120	0.556	-	-	-	-
MUCe-3D	291	41.4	1150	0.195	0.0230	< LOD	-	-
MUCe-7D	1010	114	2080	0.0580	0.282	4.34E-03	-	-
MUCe-10D	1490	167	2890	0.0360	0.534	2.96E-03	-	-
MUNd-3D	1140	189	2200	0.0900	0.441	-	2.47E-03	-
MUNd-7D	2030	387	3930	0.313	1.36	-	4.65E-03	-
MUNd-10D	4000	557	5650	0.164	3.59	-	8.03E-03	-
MUEu-3D	21.0	23.5	626	0.619	0.0210	-	-	1.71E-04
MUEu-7D	2370	195	3410	0.101	0.397	-	-	1.82E-03
MUEu-10D	2750	254	4850	0.0740	0.414	-	-	< LOD
MUCNE-3D	24.3	6.33	589	0.681	0.0120	2.53E-03	< LOD	3.55E-04
MUCNE-7D	21.9	7.59	675	0.267	0.0100	3.20E-03	< LOD	< LOD
MUCNE-10D	19.6	8.41	692	0.226	0.0140	7.41E-04	< LOD	1.46E-04

Table 11. ICP-OES results for the leachates, along with previously obtained data for REF glass and SBPW⁸. Zr concentrations are not tabulated as they remained below the detection limit for all samples.

	REF 3D	REF 7D	REF 10D	MUCe 3D	MUCe 7D	MUCe 10D	MUNd 3D	MUNd 7D	MUNd 10D	MUEu 3D	MUEu 7D	MUEu 10D	MUCNE 3D	MUCNE 7D	MUCNE 10D
NC(Si) [g/L]	0.686	1.516	1.787	1.863	6.491	9.536	7.292	13.03	25.67	0.135	15.17	17.60	0.182	0.164	0.146
f(Si) -	0.222	0.222	0.222	0.156	0.156	0.156	0.156	0.156	0.156	0.156	0.156	0.156	0.134	0.134	0.134
NL(Si) [g/m ²]	0.43	0.94	1.11	1.15	4.06	5.94	4.535	8.129	16.08	0.084	9.446	10.97	0.113	0.102	0.091
NR(Si) [g/(m ² d)]	0.142	0.134	0.111	0.385	0.580	0.594	1.512	1.161	1.608	0.028	1.349	1.097	0.038	0.015	0.009
NC(B) [g/L]	1.400	2.424	2.592	1.897	5.220	7.628	8.679	17.73	25.51	1.078	8.938	11.64	0.339	0.405	0.449
f(B) -	0.032	0.032	0.032	0.022	0.022	0.022	0.022	0.022	0.022	0.022	0.022	0.022	0.019	0.019	0.019
NL(B) [g/m ²]	0.87	1.50	1.61	1.176	3.264	4.755	5.398	11.06	15.98	0.671	5.57	7.25	0.210	0.252	0.279
NR(B) [g/(m ² d)]	0.29	0.214	0.161	0.392	0.466	0.475	1.799	1.580	1.598	0.224	0.795	0.725	0.070	0.036	0.028
NC(U) [g/L]	-	-	-	1.41E-04	1.70E-03	3.21E-03	2.65E-03	8.18E-03	2.16E-02	1.29E-04	2.39E-03	2.49E-03	1.47E-04	1.23E-04	1.72E-04
f(U) -	-	-	-	0.166	0.166	0.166	0.166	0.166	0.166	0.166	0.166	0.166	0.083	0.083	0.083
NL(U) [g/m ²]	-	-	-	8.76E-05	1.06E-03	2.00E-03	1.65E-03	5.10E-03	1.35E-02	8.03E-05	1.49E-03	1.55E-03	9.16E-05	7.65E-05	1.07E-04
NR(U) [g/(m ² d)]	-	-	-	2.92E-05	1.51E-04	2.00E-04	5.50E-04	7.29E-04	1.35E-03	2.68E-05	2.13E-04	1.55E-04	3.05E-05	1.09E-05	1.07E-05
NC(Ce) [g/L]	-	-	-	< LOD	5.33E-05	3.64E-05	-	-	-	-	-	-	3.11E-05	3.93E-05	9.10E-06
f(Ce) -	-	-	-	0.081	0.081	0.081	-	-	-	-	-	-	0.081	0.081	0.081
NL(Ce) [g/m ²]	-	-	-	-	3.33E-05	2.27E-05	-	-	-	-	-	-	1.93E-05	2.45E-05	5.65E-06
NR(Ce) [g/(m ² d)]	-	-	-	-	4.76E-06	2.27E-06	-	-	-	-	-	-	-	-	-
NC(Nd) [g/L]	-	-	-	-	-	-	2.88E-05	5.42E-05	9.37E-05	-	-	-	< LOD	< LOD	< LOD
f(Nd) -	-	-	-	-	-	-	0.086	0.086	0.086	-	-	-	0.086	0.086	0.086
NL(Nd) [g/m ²]	-	-	-	-	-	-	1.79E-05	3.38E-05	5.87E-05	-	-	-	-	-	-
NR(Nd) [g/(m ² d)]	-	-	-	-	-	-	5.97E-06	4.83E-06	5.87E-06	-	-	-	-	-	-
NC(Eu) [g/L]	-	-	-	-	-	-	-	-	-	1.98E-06	2.11E-05	< LOD	4.11E-06	< LOD	1.69E-06
f(Eu) -	-	-	-	-	-	-	-	-	-	0.086	0.086	0.086	0.086	0.086	0.086
NL(Eu) [g/m ²]	-	-	-	-	-	-	-	-	-	1.23E-06	1.31E-05	-	2.55E-06	-	1.05E-06
NR(Eu) [g/(m ² d)]	-	-	-	-	-	-	-	-	-	4.11E-07	1.87E-06	-	8.51E-07	-	1.05E-07

Table 12. Normalized concentrations, mass loss, and glass dissolution rates for si, B, U, ce, nd, and Eu in the lanthanide and uranium loaded borosilicate glass sample series were evaluated during the PCT-B test from days 3 to 10.

loaded with 30 wt% lanthanides, whereas this trend has not been observed for samples with 20 wt% U and 10 wt% lanthanides. On the other hand, the MUCNE sample displays both an expected decreasing trend and the lowest NR values observed in the study. Comparing the uranium NR values with those from earlier U loaded glass results, it is noticeable that they are generally within the same order of magnitude, except for the MUNd sample, which shows an order of 10^{-3} by the 10th day. The NC values of U are in good agreement with the results obtained in literature⁶⁶ where lower values were also measured for U than for the glass forming elements. When comparing the NR values of the surrogates with our previous lanthanide loaded glass results, we find that the values remain within the same order of magnitude, with the highest values still observed in the MUNd sample. A comparison of the NC values for Ce and Nd with data published in literature⁶⁷ reveals that the MUCe, MUNd, and MUCNE samples exhibit values an order of magnitude higher, with the exception of the 10th day result for the MUCNE sample, which falls within the same order of magnitude. The overall data suggest that the MUNd sample produces a glass with a generally weaker structure, despite containing only 60 wt% glass matrix, the MUCNE sample shows the most stable structure during leaching, outperforming the samples with higher glass matrix content.

Conclusion

Borosilicate glass matrix samples with varying compositions: 70 wt% [Matrix] combined with 20 wt% UO_3 and 10 wt% CeO_2 ; 10 wt% Nd_2O_3 ; and 10 wt% Eu_2O_3 ; and a composition of 60 wt% [Matrix] with 10 wt% UO_3 , 10 wt% CeO_2 , 10 wt% Nd_2O_3 , and 10 wt% Eu_2O_3 were synthesized and analyzed using X-ray absorption techniques, neutron diffraction coupled with RMC, and X-ray photoelectron spectroscopy were used to investigate the effects of lanthanide-uranium incorporation on the local atomic environment in the borosilicate glass. Additionally, a product consistency test was performed to assess the chemical durability of the glass specimens immersed in porewater. The U L_{III} -edge spectra were modeled with U^{VI} ions as uranyl in a linear ($\text{O}=\text{U}=\text{O}$) arrangement with six equatorial O atoms, and U^{V} in octahedral coordination. Notably, compared to the previous U containing glass samples, there was a slight increase in the $\text{U}^{\text{V}}\text{-O}$ bond length by 0.05–0.07 Å, along with increased static disorder of the U^{VO}_5 octahedra. Additionally, the structural function of Nd in the glasses is not influenced by the addition of U, Ce, or Eu. In the MUCe sample, LCF analysis confirmed 3.9% Ce^{IV} content, while the MUCNE sample showed a notable Ce^{IV} fraction (~12.3%). No redox sensitivity was observed, with Nd in the MUNd and MUCNE samples existing purely in the Nd^{III} oxidation state. Similarly, both samples containing Eu exhibited only Eu^{III} ions. LCF analysis of the U L_{III} -edge indicated no U^{IV} presence, consistently showing U^{VI} and U^{V} in similar proportions. Neutron diffraction combined with Reverse Monte Carlo simulations confirmed that the

basic structure of the mixed glass closely resembles that of the REF glass, composed of tetrahedral SiO_4 and mixed BO_3/BO_4 units. Like the U containing samples, the incorporation of both U and Ln resulted in no significant structural changes compared to the REF glass. A coordination number distribution analysis was performed to further understand B-O bonding, given the critical role of the BO_3 and BO_4 ratio in forming the basic structure of the glass matrix. While U acts as an intermediate oxide and reduces the number of four-coordinated B, Ln ions serve as modifiers, with their increasing concentration shifting the B-O coordination from 3 to 4. These findings showed that adding equal amounts of Ln ions to the basic glass structure yields similar coordination numbers. The samples show a reduction in non-bridging oxygens and promoting isomerization: $\text{BO}_3 + \text{O}^- \rightarrow [\text{BO}_4]^-$.

XPS depth analysis reveals that B concentration decreases with increasing depth, whereas the concentrations of dopants like Zr, Ce, and Ba increase. The $\text{U}^{\text{IV}}/\text{U}^{\text{VI}}$ ratio also follows a distinct pattern, with the overall U content appearing to increase as depth increases. Compared to the initial SBPW solution, the PCT test results showed increased concentrations of Si, B, and Na in all samples, indicating glass dissolution. These concentrations increased over time in each sample, with the highest levels observed in the MUNd sample.

Overall, the data suggests that the MUNd sample has a relatively weaker glass structure, while the MUCNE sample, despite containing higher, 40 wt% simulated waste components, exhibited the most stable structure during leaching, outperforming samples with higher glass matrix content.

The studied borosilicate glass matrix shows a strong capacity to incorporate high concentrations of actinides and uranium, suggesting its viability for use in high-level nuclear waste disposal.

Data availability

Datasets generated during the current study are available from the corresponding author (fabian.margit@ek.hun-ren.hu) on reasonable request.

Received: 28 April 2025; Accepted: 22 July 2025

Published online: 04 August 2025

References

- Veliscek-Carolan, J. Separation of actinides from spent nuclear fuel: A review. *J. Hazard. Mater.* **318**, 266–281 (2016).
- Necas, V. & Baratova, D. Multi-barrier system model of the geological repository for spent nuclear fuel. Proc. NUCLEAR-2016 the 9th Annual International Conference on Sustainable Development Through Nuclear Research and Education, 18–20 May 2016, Pub. Institute for Nuclear Research - Pitesti, ISSN 2066-2955, Rep Nr INIS-RO-0010, 6–12 (2016).
- Stefanovsky, S. V., Shiryaev, A. A., Zubavitchus, J. V., Veligjanin, A. A. & Marra, J. C. Valence state and speciation of uranium ions in borosilicate glasses with a high iron and aluminum content. *Glass Phys. Chem.* **35**, 141–148 (2009).
- Ojovan, M. I. & Lee, W. E. Glassy wasteforms for nuclear waste immobilization. *Metall. Mater. Trans. Phys. Metall. Mater. Sci.* **42**, 837–851 (2011).
- Lopez, C. et al. Solubility of actinide surrogates in nuclear glasses. *J. Nucl. Mater.* **312**, 76–80 (2003).
- Loiseau, P., Caurant, D., Baffier, N., Mazerolles, L. & Fillet, C. Glass–ceramic nuclear waste forms obtained from $\text{SiO}_2\text{--Al}_2\text{O}_3\text{--CaO--ZrO}_2\text{--TiO}_2$ glasses containing lanthanides (Ce, Nd, Eu, Gd, Yb) and actinides (Th): study of internal crystallization. *J. Nucl. Mater.* **335**, 14–32 (2004).
- Fabian, M. et al. Ce, Nd, Eu environments and leaching behavior in borosilicate glasses. *Sci. Rep.* **11**, 1–15 (2021).
- Tolnai, I., Osan, J., Pinakidou, E., Kovacs, Z. & Fabian, M. Effects of UO_3 on the structure, thermal and chemical stability of borosilicate glass matrix. *J. Non Cryst. Solids.* **637**, 123054 (2024).
- Fabian, M., Svab, E., Proffen, T. & Veress, E. Structure study of multi-component borosilicate glasses from high-Q neutron diffraction measurement and RMC modeling. *J. Non-cryst. Solids.* **354**, 3299–3307. <https://doi.org/10.1016/j.jnoncrsol.2008.01.024> (2008).
- Ewing, R. C., Whittleston, R. A. & Yardley, B. W. D. Geological disposal of nuclear waste: A primer. *Elements* **12**, 233–237 (2016).
- Grambow, B. Geological disposal of radioactive waste in clay. *Elements* **12**, 239–245 (2016).
- Bradbury, M. H. & Baeyens, B. A mechanistic description of Ni and Zn sorption on Na-montmorillonite part II: modelling. *J. Contam. Hydrol.* **27**, 223–248 (1997).
- Bradbury, M. H. & Baeyens, B. Derivation of In Situ Opalinus Clay Porewater Compositions from Experimental and Geochemical Modelling Studies. Technical Report Nagra 97-07, ISSN 1015-2636, 97-14 (1997).
- Varga, Z., Suranyi, G., Vajda, N. & Stefanka, Z. Determination of plutonium and americium in environmental samples by inductively coupled plasma sector field mass spectrometry and alpha spectrometry. *Microchem. J.* **85**, 39–45 (2007).
- Welter, E., Chernikov, R., Herrmann, M. & Nemausat, R. A beamline for bulk sample x-ray absorption spectroscopy at the high brilliance storage ring PETRA III. *AIP Conf. Proc.* **2054**, 040002 (2019).
- Dent, A. J. et al. B18: A core XAS spectroscopy beamline for diamond. *J. Phys. Conf. Ser.* **190**, 012039 (2009).
- Klementiev, K., Chernikov, R. & XAFSmass A program for calculating the optimal mass of XAFS samples. *J. Phys. Conf. Ser.* **712**, 012008 (2016).
- Ravel, B., Newville, M. A. T. H. E. N. A., ARTEMIS, H. E. P. H. A. E. S. T. U. S. & Data analysis for X-ray absorption spectroscopy using IFEFFIT. *J. Synchrotron Radiat.* **12**, 537–541 (2005).
- Newville, M. EXAFS analysis using FEFF and FEFFIT. *J. Synchrotron Rad.* **8**, 96–100 (2001).
- Svab, E., Meszaros, G. & Deak, F. Neutron powder diffractometer at the Budapest research reactor. *Mater. Sci. Forum.* **228–231**, 247–252 (1996).
- Cuello, G. J. et al. 7C2, the new neutron diffractometer for liquids and disordered materials at LLB. *J. Phys. Conf. Ser.* **746**, 012020 (2016).
- McGreevy, R. L. & Pusztai, L. Reverse Monte Carlo simulation: a new technique for the determination of disordered structures. *Mol. Simul.* **1**, 359–167 (1988).
- Winterer, M. Reverse Monte Carlo analysis of extended x-ray absorption fine structure spectra of monoclinic and amorphous zirconia. *J. Appl. Phys.* **88**, 5635–5644 (2000).
- Temleitner, L. et al. A new version of the RMC++ Reverse Monte Carlo programme, aimed at investigating the structure of covalent glasses. *J. Optoelectron. Adv. Mater.* **9**, 3021–3027 (2007).
- Timoshenko, J., Anspoks, A., Kalinko, A. & Kuzmin, A. Local structure of copper nitride revealed by EXAFS spectroscopy and a reverse Monte carlo/evolutionary algorithm approach. *Phys. Scr.* **91**, 054003 (2016).
- Rehr, J. J., Kas, J. J., Vila, F. D., Prange, M. P. & Jorissen, K. Parameter-free calculations of X-ray spectra with FEFF9. *Physical Chemistry Chemical Physics* **12**, 5503–5513. Preprint at <https://doi.org/10.1039/b926434e> (2010).

27. Fabian, M. et al. Network structure of 0.7SiO₂-0.3Na₂O glass from neutron and x-ray diffraction and RMC modelling. *J. Phys. Condens. Matter.* **19**, 335209 (2007).
28. Svab, E., Fabian, M., Veress, E. & Proffen Th. Short- and intermediate range order in borosilicate waste glasses. *Acta Crystallogr. A.* **61**, 58–59 (2007).
29. Fabian, M. et al. Structural investigation of borosilicate glasses containing lanthanide ions. *Sci. Rep.* **10**, 1–14 (2020).
30. Standard Test Methods for Determining Chemical Durability of nuclear, hazardous, and mixed waste glasses and multiphase glass ceramics: the product consistency test (PCT). (2021). <https://doi.org/10.1520/C1285-21>
31. Varga, A., Raucsik, B., Szakmany, G. & Mathe, Z. Mineralogical, petrological and geochemical characteristics of the siliciclastic rock types of Boda siltstone formation. *Földtani Kozlony.* **136**, 1–31 (2006).
32. Breitner, D. et al. Characteristics of uranium uptake of Boda claystone formation as the candidate host rock of high level radioactive waste repository in Hungary. *Environ. Earth Sci.* **73**, 209–219 (2015).
33. Praveena, N. et al. Studies on chemical state of uranium in modified sodium borosilicate glass using X-ray photoelectron spectroscopy and X-ray absorption spectroscopy. *Prog. Nucl. Energy.* **131**, 119726 (2021).
34. El-Damrawi, G. & Behairy, A. Structural role of cerium oxide in lead silicate glasses and glass ceramics. *J. Minerals Mater. Charact. Eng.* **06**, 438–447 (2018).
35. Cicconi, M. R., Veber, A., Neuville, D. R., Baudelet, F. & de Ligny, D. Cerium speciation in silicate glasses: Structure-property relationships. *J. Non Cryst. Solids.* **563**, 120785 (2021).
36. Laves, F., Lshberg, K., Rahlfs, P., Kasper, J. S. & Roberts, B. *Dezember 1969 und 16. Math:Phys KI* vol. 67 (1970).
37. The Materials Project. Materials data on Eu₂Si₂O₇ by materials project. *United States: N P.* <https://doi.org/10.17188/1197025> (2020).
38. Goriounova, A., Held, P., Becker, P. & Bohatý, L. Europium triborate, EuB₃O₆. *Acta Crystallogr. Sect. E Struct. Rep. Online.* **60**, 131–133 (2004).
39. Revisited, C., Tas, S. A. & Akinc, M. Crystal structures of the High-Temperature forms of Ln₂Si₂O₇ (Ln = La, Ce, Pr, Nd, Sm) revisited. *J. Am. Ceram. Soc.* **77**, 2968–2970 (1994).
40. Wang, Y. et al. Effect of neodymium on the glass formation, dissolution rate and crystallization kinetic of borophosphate glasses containing iron. *J. Non Cryst. Solids.* **526**, 119726 (2019).
41. Cicconi, M. R. et al. Europium oxidation state and local structure in silicate glasses. *Am. Mineral.* **97**, 918–929 (2012).
42. Matyunin, Y. I. & Yudinsev, S. V. Immobilization of U₃O₈ in borosilicate glass in an induction melter with a cold crucible. *At. Energ.* **84**, 173–178 (1998).
43. Sanyal, K., Khooha, A., Das, G., Tiwari, M. K. & Misra, N. L. Direct determination of oxidation States of uranium in Mixed-Valent uranium oxides using total reflection X-ray fluorescence X-ray absorption Near-Edge spectroscopy. *Anal. Chem.* **89**, 871–876 (2017).
44. Charfi, B., Zekri, M., Herrmann, A., Damak, K. & Maâlej, R. Atomic scale network structure of a barium aluminosilicate glass doped with different concentrations of rare-earth ions explored by molecular dynamics simulations. *Comput. Mater. Sci.* **218**, 111965 (2023).
45. Du, J. & Cormack, A. N. The structure of erbium doped sodium silicate glasses. *J. Non Cryst. Solids.* **351**, 2263–2276 (2005).
46. Wilding, M., Badyal, Y. & Navrotsky, A. The local environment of trivalent lanthanide ions in sodium silicate glasses: A neutron diffraction study using isotopic substitution. *J. Non Cryst. Solids.* **353**, 4792–4800 (2007).
47. Bouty, O., Delaye, J. M., DeBonfils, J. & Peugeot, S. WAXS investigation of lanthanide borosilicate glasses. *ATALANTE 2008: Nuclear Fuel Cycle for a Sustainable Future* (2008).
48. Park, B., Li, H., Ren, E. E. & Corrales, L. Molecular dynamics simulation of La₂O₃-Na₂O-SiO₂ glasses: the structure role of La³⁺ + Cations. *J. Non Cryst. Solids.* **297**, 220–238 (2002).
49. Rino, J. P., Ebbsjo, I., Kalia, R. K., Nakano, A. & Vashishta, P. Structure of rings in vitreous SiO₂. *Phys. Rev. B.* **47**, 3053–3062 (1993).
50. Qian, M., Li, H., Li, L. & Strachan, D. M. Extended electron energy loss fine structure simulation of the local Boron environment in sodium aluminoborosilicate glasses containing gadolinium. *J. Non Cryst. Solids.* **328**, 90–101 (2003).
51. Connelly, A. J. et al. The effect of uranium oxide additions on the structure of alkali borosilicate glasses. *J. Non Cryst. Solids.* **378**, 282–289 (2013).
52. El-Damrawi, G., Gharghar, F. & Ramadan, R. More insight on structure of new binary cerium Borate glasses. *New. J. Glass Ceram.* **08**, 12–21 (2018).
53. Burns, A. E. et al. Structure of binary neodymium Borate glasses by infrared spectroscopy. *J. Non Cryst. Solids.* **352**, 2364–2366 (2006).
54. Du, L. S. & Stebbins, J. F. Solid-state NMR study of metastable immiscibility in alkali borosilicate glasses. *J. Non Cryst. Solids.* **315**, 239–255 (2003).
55. Fabian, M., Proffen, T., Ruett, U., Veress, E. & Svab, E. Uranium surroundings in borosilicate glass from neutron and x-ray diffraction and RMC modelling. *Journal Phys. Condens. Matter* **22**, (2010).
56. Fabian, M. & Araczk, C. Basic network structure of SiO₂-B₂O₃-Na₂O glasses from diffraction and reverse Monte Carlo simulation. *Phys Scr* **91**, (2016).
57. Fabian, M., Svab, E. & Zimmermann, M. V. M. V. Structure study of new uranium loaded borosilicate glasses. *J. Non Cryst. Solids.* **380**, 71–77 (2013).
58. Jollivet, P., Den Auwer, C. & Simoni, E. Evolution of the uranium local environment during alteration of SON68 glass. *J. Nucl. Mater.* **301**, 142–152 (2002).
59. Farges, S., Ponader, C. W., Calas, G. & Brown, G. E. Jr Structural environments of incompatible elements in silicate glass/melt systems: II. UIV, UV, and UVI. *Geochim. Cosmochim. Acta.* **56**, 4205–4220 (1992).
60. Zhang, F., Wang, P., Koberstein, J., Khalid, S. & Chan, S. W. Cerium oxidation state in ceria nanoparticles studied with X-ray photoelectron spectroscopy and absorption near edge spectroscopy. *Surf. Sci.* **563**, 74–82 (2004).
61. Paparazzo, E. XPS studies of damage induced by X-ray irradiation on CeO₂ surfaces. *Surf. Sci. Lett.* **234**, 253–258 (1990).
62. Ilton, E. S., Boily, J. F. & Bagus, P. S. Beam induced reduction of U(VI) during X-ray photoelectron spectroscopy: the utility of the U_{4f} satellite structure for identifying uranium oxidation States in mixed Valence uranium oxides. *Surf. Sci.* **601**, 908–916 (2007).
63. Ilton, E. S. et al. Quantifying small changes in uranium oxidation States using XPS of a shallow core level. *Phys. Chem. Chem. Phys.* **19**, 30473–30480 (2017).
64. Malik, P. P. Maity. Synthesis and leaching behaviour of borosilicate glasses containing uranium as radioactive waste. *J. Indian Chem. Soc.* **97**, 2909–2913 (2020).
65. Thorat, V. S. et al. Corrosion of borosilicate glasses subjected to aggressive test conditions: structural investigations. *J. Am. Ceram. Soc.* **99**, 3251–3259 (2016).
66. Maeda, T., Banba, T., Sonoda, K., Inagaki, Y. & Furuya, H. Release and retention of uranium during glass corrosion. *J. Nucl. Mater.* **298**, 163–167 (2001).
67. Kim, M. & Heo, J. Calcium-borosilicate glass-ceramics wasteforms to immobilize rare-earth oxide wastes from pyro-processing. *J. Nucl. Mater.* **467**, 224–228 (2015).

Acknowledgements

One of the authors (M.F.) acknowledges that this project was partly supported by the János Bolyai Research

Scholarship of the Hungarian Academy of Sciences. The authors would like to thank Laboratoire Leon Brillouin for beamtime (proposal Nr. 12426) and the J. Darpentigny for assistance with measurements and data collection. The authors would like to thank Diamond Light Source for beamtime (proposal SP33573), and the staff of beamlines B18 for assistance with measurements and data collection. The authors would like to thank DESY: PETRA III for beamtime (proposal I-20220782), and the staff of beamlines P65 for assistance with measurements and data collection. P.J. is indebted to D. Zalka (Solaris Synchrotron, Krakow) for helpful discussions.

Author contributions

I. Tolnai: Writing – original draft, Investigation, Data curation. J. Osan: Investigation, Data curation, Writing – review & editing. P. Jovari: Data curation, Writing – review & editing. F. Pinakidou: Data curation. A. Sulyok: Investigation, Data curation, Writing – review & editing. M. Fabian: Conceptualization, Investigation, Data curation, Writing – review & editing. All authors reviewed the manuscript.

Funding

Open access funding provided by HUN-REN Centre for Energy Research.

Declarations

Competing interests

The authors declare no competing interests.

Ethics declarations

Not applicable.

Supplementary Information

Supplementary material available, calculated surface concentrations, variations in the % of U^{IV} relative to the atomic number of the lanthanides, the region of Nd peak detected on the MUND sample.

Additional information

Supplementary Information The online version contains supplementary material available at <https://doi.org/10.1038/s41598-025-13166-1>.

Correspondence and requests for materials should be addressed to M.F.

Reprints and permissions information is available at www.nature.com/reprints.

Publisher's note Springer Nature remains neutral with regard to jurisdictional claims in published maps and institutional affiliations.

Open Access This article is licensed under a Creative Commons Attribution 4.0 International License, which permits use, sharing, adaptation, distribution and reproduction in any medium or format, as long as you give appropriate credit to the original author(s) and the source, provide a link to the Creative Commons licence, and indicate if changes were made. The images or other third party material in this article are included in the article's Creative Commons licence, unless indicated otherwise in a credit line to the material. If material is not included in the article's Creative Commons licence and your intended use is not permitted by statutory regulation or exceeds the permitted use, you will need to obtain permission directly from the copyright holder. To view a copy of this licence, visit <http://creativecommons.org/licenses/by/4.0/>.

© The Author(s) 2025